

## PAPER

Cite this: *RSC Adv.*, 2016, 6, 33433

# Enhanced photovoltage in DSSCs: synergistic combination of a silver modified TiO<sub>2</sub> photoanode and a low cost counter electrode

 Samim Sardar,<sup>a</sup> Srabanti Ghosh,<sup>\*a</sup> Hynd Remita,<sup>b</sup> Prasenjit Kar,<sup>a</sup> Bo Liu,<sup>c</sup> Chinmoy Bhattacharya,<sup>e</sup> Peter Lemmens<sup>cd</sup> and Samir Kumar Pal<sup>\*a</sup>

In this study, we have tailored both the active electrode with silver modified TiO<sub>2</sub> (Ag–TiO<sub>2</sub>) as well as the counter electrode (CE) with Pt–reduced graphene oxide (Pt@RGO) nanocomposites to realize efficient and low cost devices. The synergistic combination of both modified electrodes leads to an improved light to electrical energy conversion with an overall efficiency of 8%. An increase in the photovoltage ( $V_{OC}$ ) of ~16% (0.74 to 0.86 V) is achieved using Ag–TiO<sub>2</sub> in comparison to the bare TiO<sub>2</sub>. This can be attributed to the shifting of the quasi-Fermi level of the TiO<sub>2</sub> photoanode close to the conduction band in the presence of Ag nanoparticles (NPs) due to the formation of the Schottky barrier. On the other hand, the facile synthesis of Pt NPs on RGO nanosheets by a photo-reduction method without using chemical reducing or stabilizing agents demonstrates a higher efficiency than Pt as a CE due to the cooperation of the catalytic activity of Pt and the high electron conductivity of the RGO as a stable supporting material having more interfacial active sites. The quantity of Pt in the Pt@RGO nanocomposites is 10 times lower than in the Pt CE which reduces the cost and makes it viable for large scale commercial utilization.

Received 21st January 2016

Accepted 28th March 2016

DOI: 10.1039/c6ra01863g

www.rsc.org/advances

## 1. Introduction

Solar energy is the most promising resource to meet future energy demands due to the depletion of fossil fuels. Among various technologies, dye-sensitized solar cells (DSSCs) have attracted widespread attention as a solar energy conversion technology because of abundantly available low cost materials, ease of fabrication and relatively high photon to current conversion efficiency.<sup>1</sup> DSSCs consist of a nanocrystalline porous semiconductor electrodes-sensitized with light absorbing dye as a photoanode, I<sup>-</sup>/I<sub>3</sub><sup>-</sup> or Co<sup>2+</sup>/Co<sup>3+</sup> redox couples as electrolytes and platinized conducting glass as counter electrode (CE).<sup>1a</sup> Extensive efforts have been made to improve the efficiency of DSSC by engineering all the components. For instance, nanocrystalline TiO<sub>2</sub> films with various morphologies<sup>2</sup> and dopants,<sup>3</sup> synthesizing panchromatic dyes to absorb visible and near-infrared light effectively,<sup>4</sup> synthesizing alternative redox electrolytes<sup>5</sup> and substituting platinized

counter electrodes with low cost materials<sup>6</sup> have all been explored to enhance the photocurrent and photovoltage, in order to improve the efficiency of DSSCs.

Among all the factors, the photoanode is regarded as sovereign for improving the efficiency. In order to modulate the photoanode, thickness of the nanocrystalline titanium dioxide layer has been extensively studied to improve both the photocurrent and photovoltage.<sup>7</sup> Generally lowering the thickness of the active layer reduces the recombination at the interface between electrode and electrolyte which in turn increases the efficiency. However, the dye loading also decreases with decreasing thickness resulting in lower photocurrents. To combat this problem, surface modification of semiconductor nanoparticles (NPs) with plasmonic metal nanostructures such as gold, silver and copper have been investigated recently.<sup>8</sup> Solar cells employing hybrid materials have revolutionized efficient solar energy conversion applications through cost-effective fabrication techniques.<sup>9</sup> Hupp *et al.* reported the enhancement of photocurrent in DSSC by the localized surface plasmon resonance (SPR) of silver NPs which increases the effective absorption cross section of dye molecules.<sup>8a,10</sup> The enhancement of photocurrents in DSSC by using silver doped semiconductor nanostructures are well documented in the literature.<sup>11</sup> But significant improvement of the photovoltage by surface modification with silver is reported sparsely in the literature. Recently, Kamat *et al.*<sup>12</sup> have reported significant photovoltage boosting of DSSC with thiolated gold nanocluster anchored on TiO<sub>2</sub> surface along with squaraine as a sensitizing

<sup>a</sup>Department of Chemical, Biological and Macromolecular Sciences, S. N. Bose National Centre for Basic Sciences, Block JD, Sector III, Salt Lake, Kolkata 700 098, India. E-mail: srabanti.ghosh@bose.res.in; skpal@bose.res.in

<sup>b</sup>CNRS, Laboratoire de Chimie Physique, UMR 8000, Université Paris-Sud, 91405 Orsay, France

<sup>c</sup>Institute for Condensed Matter Physics, TU Braunschweig, Mendelssohnstraße 3, 38106 Braunschweig, Germany

<sup>d</sup>Laboratory for Emerging Nanometrology, TU Braunschweig, Braunschweig, Germany

<sup>e</sup>Department of Chemistry, Indian Institute of Engineering Science and Technology Shibpur, P.O. Botanic Garden, Howrah-711103, India

dye. Gold nanoclusters increase the quasi-Fermi level of TiO<sub>2</sub> close to the conduction band which enhances the open circuit photovoltage. In the present study, we aimed to raise the photovoltage of DSSC by silver modification on TiO<sub>2</sub> surface as well as modification of CE with low cost materials.

Another aspect in order to realize the cost effective DSSCs is the development of alternative counter electrode materials. In DSSC, the most prevailing CE is a platinum (Pt) thin film due to its exceptionally high electrochemical activity.<sup>13</sup> However, the high cost and corrosion of Pt in presence of the iodine electrolyte restricts it from large scale applications and long term use.<sup>14</sup> In this regard, carbon based materials such as carbon nanotube, graphene and reduced graphene oxide (RGO) as CE have induced current research interests as a substituent of Pt due to low cost, high charge carrier mobility<sup>15</sup> and reasonable performances.<sup>16</sup> However, the energy conversion efficiency is lower in case of graphene CE compared to that of Pt electrodes and also requires large quantities of graphene to achieve an acceptable catalytic activity.<sup>16a,17</sup> Thus hybridization of small amount of Pt with graphene or reduced graphene oxide can meet the requirements of low cost, long term stability as well as high catalytic activity. Significant efforts have been made to fabricate Pt NPs on reduced graphene oxide film or substrate by using chemical reducing agents,<sup>18</sup> photo-reduction,<sup>19</sup> pulsed laser ablation method,<sup>20</sup> dry plasma reduction,<sup>6a</sup> thermal decomposition<sup>21</sup> and hydrogen plasma<sup>22</sup> *etc.* However, in most cases, the energy conversion efficiency has not reached the expected level as well as the complex fabrication process limits its large scale application. The modification of both the active and counter electrode can provide both high efficiency and low cost requirements which indeed remain unexplored in the contemporary literature.

In the present study, we have modified both the active and counter electrodes to realize an energy efficient device using simple fabrication processes. We have synthesized and characterized small silver NPs embedded on the TiO<sub>2</sub> surface (Ag-TiO<sub>2</sub>) as a photoanode material which exhibits significant enhancement in the photovoltage. On the other hand, the CE has been modified with the Pt NPs supported on RGO (Pt@RGO) using a facile photo-reduction method without any reducing or stabilizing agents where Pt loading is very low compared to that of the standard Pt CE. This reduces the cost and also increases the catalytic activity to regenerate the electrolyte more efficiently. The combination of both factors enhances the efficiency of the device as high as 8%. The open circuit photovoltage decay measurement in the presence of Ag-TiO<sub>2</sub> photoanode unravels slow back electron transfer from the active layer to the electrolyte or oxidized dye molecules. The present study will be helpful in designing an easy fabrication process of low cost, efficient and large scale production of future solar devices.

## 2. Experimental section

### 2.1. Reagents

TiO<sub>2</sub> (P25) was purchased from Evonik. Platinum chloride (H<sub>2</sub>PtCl<sub>6</sub>), silver perchlorate (AgClO<sub>4</sub>), platinum(II) acetylacetonate

(Pt(C<sub>5</sub>H<sub>7</sub>O<sub>2</sub>)<sub>2</sub>), di-tetrabutylammonium *cis*-bis(isothiocyanato) bis(2,2'-bipyridyl-4,4'-dicarboxylato)ruthenium(II) (N719), lithium iodide (LiI), iodine (I<sub>2</sub>) and 4-*tert*-butylpyridine (TBP) were purchased from Sigma-Aldrich. Ultrapure water (Millipore System, 18.2 MΩ cm) and ethanol (≥99% for HPLC, purchased from Sigma-Aldrich) were used as solvents. Analytical-grade chemicals were used for synthesis without further purifications. Fluorine-doped tin oxide (FTO) conducting glass substrates, acquired from Sigma-Aldrich were cleaned by successive sonication with soap water, acetone, ethanol and deionized (DI) water for 15 min, each with adequate drying prior to their use.

### 2.2. Synthesis of silver modified TiO<sub>2</sub>

The Ag-TiO<sub>2</sub> samples were obtained by radiolytic reduction of Ag<sup>+</sup> in the TiO<sub>2</sub> suspension following our previous report.<sup>23</sup> An ethanolic solution of AgClO<sub>4</sub> ( $2 \times 10^{-3}$  M) and TiO<sub>2</sub> (Evonik P25) suspension is sonicated for 3 min, then degassed with nitrogen and irradiated (under stirring) with a <sup>60</sup>Co panoramic gamma source (dose rate, 2.3 kGy h<sup>-1</sup>). The silver ions were reduced by the solvated electrons and the alcohol radicals induced by solvent radiolysis under 1 h 20 min irradiation to reduce all the silver ions. The Ag-TiO<sub>2</sub> samples were centrifuged and dried at 60 °C.

### 2.3. Synthesis of Pt NPs supported on reduced graphene oxide

The graphene oxide (GO) was synthesized from graphite powder by the modified Hummers method as reported in our previous publication.<sup>24</sup> The GO (1 mg mL<sup>-1</sup>) was then dispersed in 2-propanol and exfoliated in an ultrasonic bath for 20 min. Then 1 mM of platinum(II) acetylacetonate was added to the GO dispersion followed by deoxygenation under a N<sub>2</sub> flow. Then the mixture was irradiated under UV light for 6 h under a N<sub>2</sub> atmosphere.<sup>25</sup> Then as synthesized Pt-reduced graphene oxide nanohybrid was centrifuged and dried at 60 °C. The reduced GO was synthesized following the same procedure without adding the platinum salt.

### 2.4. Fabrication of DSSCs

For the fabrication of DSSCs, platinum, Pt@RGO and RGO deposited on FTO substrates were used as counter electrodes. The platinum (Pt) were deposited on the FTO substrates by thermal decomposition of 5 mM platinum chloride (in isopropanol) at 385 °C for 30 min. The N719 coated TiO<sub>2</sub> and Ag-TiO<sub>2</sub> were used as the photo anodes and the two electrodes were placed on top of each other with a single layer of 60 μm thick Surlyn (Solaronix) as a spacer between the two electrodes. A liquid electrolyte composed of 0.5 M lithium iodide (LiI), 0.05 M iodine (I<sub>2</sub>) and 0.5 M 4-*tert*-butylpyridine (TBP) in acetonitrile was used as the hole conductor and filled in the inter electrode space by using capillary force, through two small holes (diameter = 1 mm) predrilled on the counter electrode. Finally, the two holes were sealed by using another piece of Surlyn to prevent the leakage of electrolyte from the cell. In all our experiments, the active area of the DSSCs was fixed at 0.49 cm<sup>2</sup>.

## 2.5. Characterization methods

Field Emission Scanning Electron Microscopy (FESEM, QUANTA FEG 250) was used to investigate the surface morphology of the samples. Transmission electron microscopy (TEM) was carried out using an FEI (Technai S-Twin) instrument with acceleration voltage of 200 kV. A drop of sample was placed on a carbon-coated copper grid and particle sizes were determined from micrographs recorded at a high magnification of 100 000 $\times$ . The Pt content in Pt@RGO nanocomposite was determined by inductively coupled plasma-mass spectrometry (ICP-MS). The solvent was first evaporated and samples were mineralized using 5 mL of aqua regia and injected. After 20 times dilution with ultrapure water, *via* a peristaltic pump at 0.1 mL min<sup>-1</sup> flow rate, nebulization of samples was performed by means of a micro concentric nebulizer (Micromist). A 7500 ce ICP-MS (Agilent) was used as the elemental detector. Detection of Pt was performed by selecting abundant isotopes free of interferences, *i.e.*, <sup>194</sup>Pt and <sup>195</sup>Pt. X-ray diffraction (XRD) was used to characterize crystal phase by a PANalytical XPERTPRO diffractometer equipped with Cu K $\alpha$  radiation (at 40 mA and 40 kV) at a scanning rate of 0.02 $^\circ$  s<sup>-1</sup> in the 2 $\theta$  range from 20 $^\circ$  to 80 $^\circ$ . Raman scattering experiments were carried out by a Micro Raman setup (Horiba LabRAM) with the excitation wavelength of 532 nm at room temperature. Thermal gravimetric analysis (TGA) of GO, RGO and Pt@RGO solid powder was performed under nitrogen atmosphere with a heating rate of 10  $^\circ$ C min<sup>-1</sup> from 30  $^\circ$ C to 900  $^\circ$ C by using a Perkin-Elmer TGA-50H. The current density–voltage characteristics of the cells were recorded by a Keithley multimeter under irradiance of 100 mW cm<sup>-2</sup> (AM 1.5 simulated illuminations, Photo Emission Tech). The fill factor (FF) and power conversion efficiency ( $\eta$ ) of the solar cells are determined from eqn (1) and (2),

$$FF = V_M J_M / V_{OC} J_{SC} \quad (1)$$

$$\eta = V_{OC} J_{SC} FF / P_{in} \quad (2)$$

where  $V_M$  and  $J_M$  are the voltage and current density at the maximum power output, respectively.  $J_{SC}$  and  $V_{OC}$  are the short-circuit photocurrent density and open-circuit photovoltage, and  $P_{in}$  is the intensity of the incident light (100 mW cm<sup>-2</sup>). The incident photon-to-current conversion efficiency (IPCE) was evaluated by measuring short-circuit photocurrent ( $J_{SC}$ ) at different wavelengths ( $\lambda$ ) using a homemade setup with a Bentham monochromator and dual light (tungsten and xenon) sources. The IPCE was calculated using eqn (3),

$$IPCE\% = [1240 \times J_{SC} (\text{A cm}^{-2})] / [\lambda (\text{nm}) \times P (\text{W cm}^{-2})] \times 100 \quad (3)$$

where,  $P$  is the incident light power.

Photovoltage decay measurements were carried out after illuminating the cells under 1 Sun condition. The photovoltage decays after switching off the irradiation were monitored by an oscilloscope (Owon) through computer interface. The decays were fitted with exponential decay functions using origin software. Electrochemical impedance spectroscopy (EIS) were performed

on an electrochemical workstation CHI650E (CH instruments) with a frequency range from 100 kHz to 0.1 Hz in the open circuit condition. All impedance measurements were carried out under a bias illumination of 100 mW cm<sup>-2</sup>. The obtained spectra were fitted using the CHI650E software in terms of appropriate equivalent circuits.

## 3. Results and discussion

The formation of silver modified TiO<sub>2</sub> (Ag–TiO<sub>2</sub>) by radiolysis and detailed characterization are reported in our previous publication.<sup>23</sup> The silver ions were reduced by the free radicals such as solvated electrons and alcohol radicals generated due to high energy radiation. The silver nanoparticles (NPs) (2% metal loading) are homogeneously distributed on P25 TiO<sub>2</sub> NPs as shown in a Transmission Electron Microscopic image (Fig. 1a). The average size of the silver NPs is 2 nm. The elemental distribution of the Ag–TiO<sub>2</sub> was further characterized by energy dispersive spectroscopic (EDS) mapping. The EDS elemental mapping clearly confirmed the presence and homogeneous distribution of Ag, Ti, and O elements in the Ag–TiO<sub>2</sub> as shown in Fig. 1b. The EDS spectrum indicates the presence of 1.61% Ag in the material (Fig. 1c).

In order to lower the Pt content in CE which in turn decreases the cost, small amount of Pt has been hybridized with RGO (Pt@RGO). The simultaneous photo-reduction of GO and Pt salt under UV light irradiation without any chemical reducing or stabilizing agents results in the successful formation of the nanohybrid. In hydrogen-donating solvents, Pt(acac)<sub>2</sub> undergoes efficient photodegradation to yield colloidal platinum. The photoreduction mechanism of Pt(acac)<sub>2</sub> in alcohol solution has been established in our previous publication.<sup>25</sup> Fig. 2a and b illustrate the scanning electron microscopic (SEM) images of RGO and Pt NPs on the RGO, respectively. The homogeneous distribution of Pt NPs all over the RGO nanosheet is clearly evident from the TEM image as shown in Fig. 2c. The average particle size of Pt NPs is estimated by fitting the experimental TEM data over 200 particles and it is found to be 2.6 nm as shown in the inset of Fig. 2c. From high resolution TEM (HR-TEM) image of Pt@RGO, the inter-planar distance between the fringes of Pt NPs is found to be about 0.234 nm which is consistent with (111) planes (Fig. 2d).<sup>20</sup> The crystal planes of the RGO nanosheets are also evident from the HR-TEM image. The Pt content in Pt@RGO nanocomposite has been estimated from the ICP-MS and it is found to be 20.7%.

The X-ray diffraction patterns (XRD) of GO, RGO and Pt@RGO are presented in Fig. 3a. The GO sample shows characteristic diffraction peaks at 25.9 $^\circ$  and 42.3 $^\circ$  which can be assigned to the (002) and (100) crystal planes, respectively. In case of RGO and Pt@RGO, the peak at 25.9 $^\circ$  moved slightly to a higher angle which indicates the partial reduction of GO to the conjugated crystalline graphene network (sp<sup>2</sup>).<sup>26</sup> The peak at 42.3 $^\circ$  corresponding to the (100) planes diminishes after the deposition of Pt on RGO nanosheets due to the surface coverage by Pt NPs.<sup>27</sup> In addition, the peaks of the Pt@RGO nanocomposites at 39.8 $^\circ$ , 46.5 $^\circ$  and 67.5 $^\circ$  can be assigned to the (111), (200) and (220) crystal planes of face centered-cubic (fcc) Pt NPs, respectively. The results confirm the successful

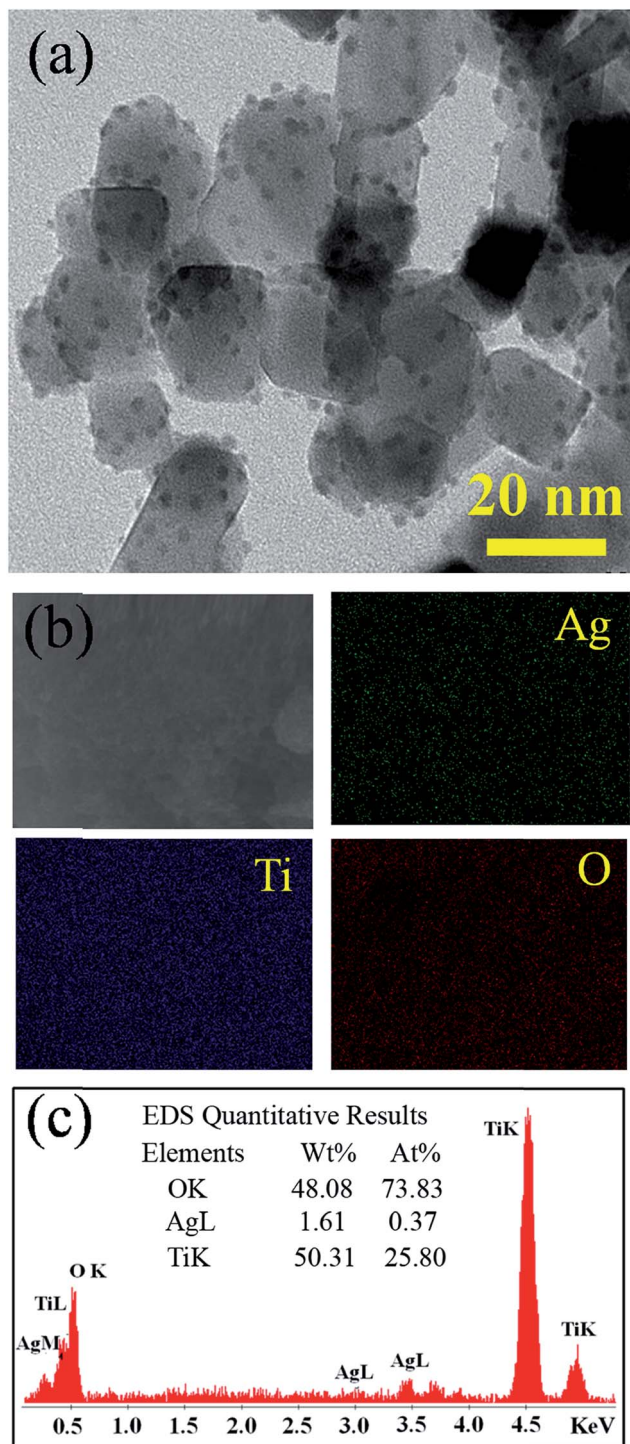


Fig. 1 Characterization of Ag–TiO<sub>2</sub> nanocomposites. (a) TEM image of silver modified TiO<sub>2</sub>. (b) SEM image and Ag, Ti, O elemental mapping images of Ag–TiO<sub>2</sub> nanocomposites. (c) EDAX spectrum of Ag–TiO<sub>2</sub> nanocomposites.

formation of Pt NPs over the RGO nanosheets. To further characterize the nanocomposites, Raman spectra of GO, RGO and Pt@RGO have been collected as shown in Fig. 3b. The Raman spectra show two major peaks, a G band at 1590 cm<sup>-1</sup> and a D band at 1352 cm<sup>-1</sup>. The G band corresponds to the in

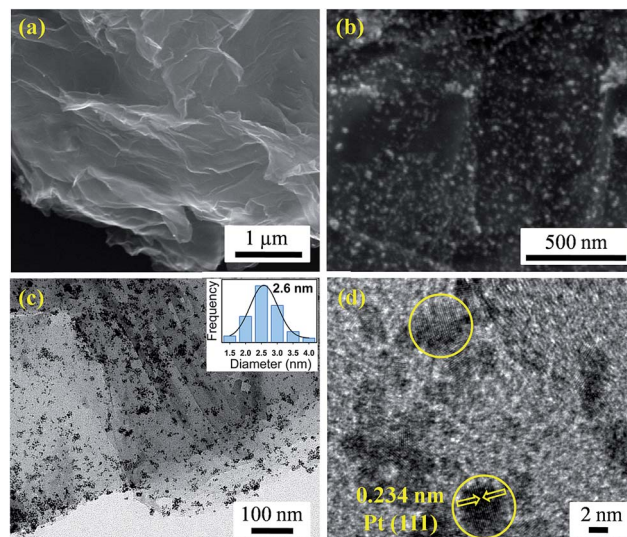


Fig. 2 Electron microscopic images of the Pt@RGO nanocomposites. SEM images of (a) RGO nanosheets and (b) Pt@RGO nanocomposites. (c) TEM and (d) HRTEM images of Pt@RGO nanocomposites. Inset of (c) shows the size distribution of the Pt NPs on RGO nanosheets.

plane bond stretching motion of pairs of C sp<sup>2</sup> atoms (E<sub>2g</sub> mode), while D band corresponds to the disordered structures, such as bond angle disorders and asymmetric lattices in the graphite.<sup>6a,18</sup> The intensity ratio of D band to G band (D/G) increases after reduction of GO to RGO and further increases after the formation of the nanocomposite. The increase in D/G intensity ratio can be attributed to (a) an increase in the quantity of amorphous carbon, (b) a higher density of defects on the structure, or (c) a reduction in the crystallite size or domains.<sup>28</sup> In the present case, the increase in the intensity ratio may be due to the increase in the density of defects on the graphene structures after deposition of Pt NPs. In case of Pt@RGO, a strong D' peak at 1615 cm<sup>-1</sup> is observed, which can be assigned to the nonzero phonon density of the states at energies above the energy of the G band. These phonons are usually Raman-inactive but become active due to phonon confinement caused by the defects.<sup>29</sup> Moreover, thermogravimetric analysis has been carried out to assess the thermal stability of the nanocomposite as shown in Fig. 3c. For the GO sample, a weight loss of ~40% occurs between 180 to 230 °C due to a pyrolysis of the labile oxygen-containing functional groups, yielding CO, CO<sub>2</sub> and steam.<sup>30</sup> The weight loss in the similar temperature range for the RGO and Pt@RGO decreases to ~33% and 27%, respectively. This observation indicates the decrease of functional groups in the RGO and Pt@RGO samples after reduction. The complete decomposition of the GO and RGO samples occurs around 500 °C, while the carbonaceous material present in the Pt@RGO decomposes around 400 °C. The lower decomposition temperature can be attributed to an increase in the interlayer distance of the nanosheets due to the presence of Pt NPs. A residue of ~20% remains at high temperature in case of Pt@RGO due to the presence of Pt NPs which is well consistent with the ICP-MS data.

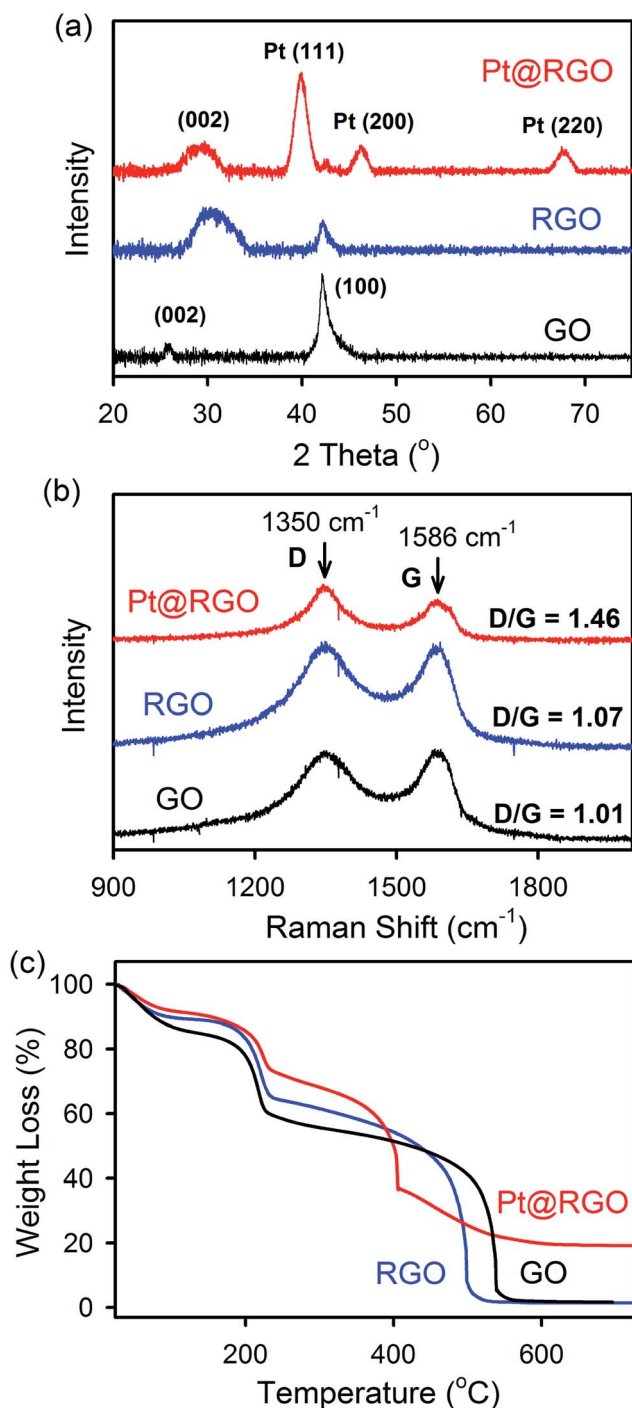


Fig. 3 Characterization of the Pt@RGO nanocomposites. (a) X-ray diffraction patterns (b) Raman spectra and (c) thermogravimetric analysis profiles of Pt@RGO (red), RGO (blue) and GO (black).

In order to demonstrate practical applications utilizing Ag-TiO<sub>2</sub> at active electrode and Pt@RGO at counter electrode, a series of DSSCs were fabricated. Fig. 4a shows the photocurrent-voltage characteristics of DSSCs fabricated with different active and counter electrodes. The corresponding values of the photovoltaic parameters, such as the short circuit photocurrent density ( $J_{SC}$ ), open circuit voltage ( $V_{OC}$ ), fill factor (FF), power

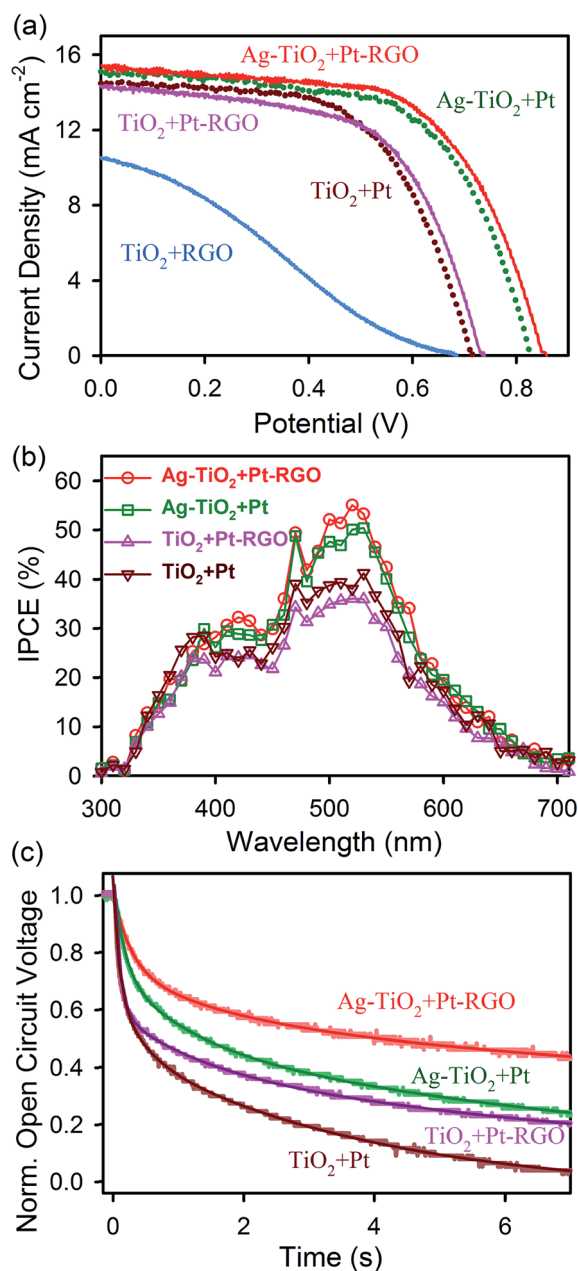


Fig. 4 Device performance. (a)  $J$ - $V$  characteristics, (b) incident photon to current conversion efficiency (IPCE) spectra and (c) open circuit voltage decay profiles of different DSSCs.

conversion efficiency ( $\eta$ ) for the best cells along with the average efficiency values are presented in Table 1. An increase of around 16% (from 0.72 to 0.84 V) in the photovoltage ( $V_{OC}$ ) is observed in case of Ag-TiO<sub>2</sub> at photoanode compared to that of the bare TiO<sub>2</sub> along with Pt at the counter electrode. During steady state illumination,  $V_{OC}$  is the difference in potential between the quasi-Fermi level of the TiO<sub>2</sub> film and the rest potential of the counter electrode, which remains in equilibrium with the redox couple. Semiconductor and metal NPs undergo electron equilibration under light illumination. In the Ag-TiO<sub>2</sub> nanocomposites, due to the larger work function of Ag (4.5–4.7 eV)<sup>31</sup> compared to the electron affinity of TiO<sub>2</sub> (1.59 eV),<sup>32</sup> a Schottky

Table 1 Solar cell performance using different active and counter electrodes<sup>a</sup>

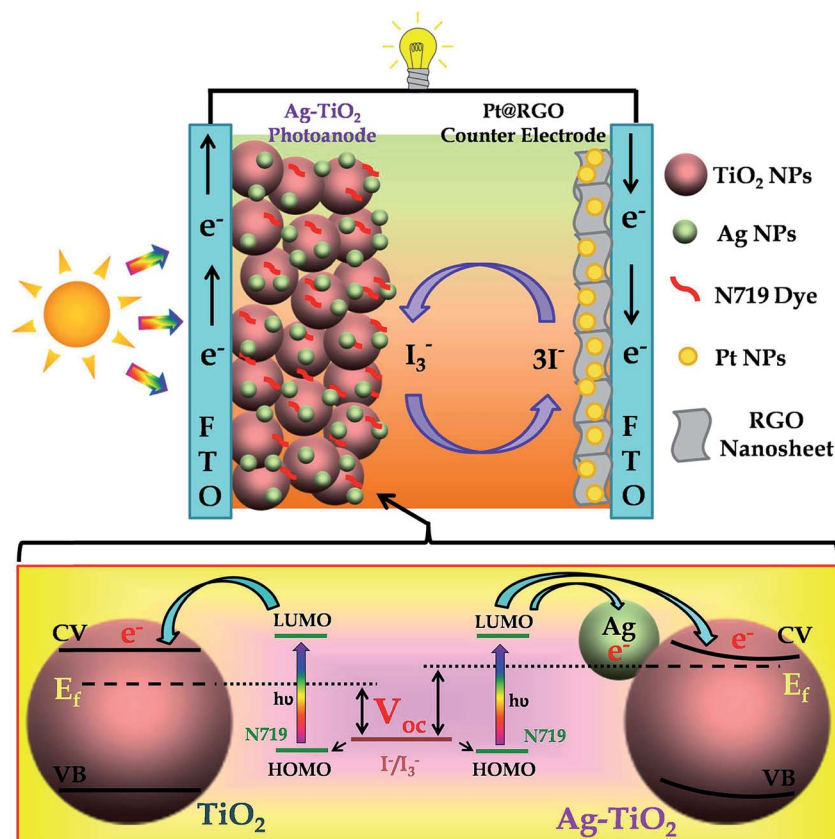
Photoanode	Counter electrode	Best values				Average value $\eta$ (%)
		$J_{SC}$ (mA cm <sup>-2</sup> )	$V_{OC}$ (V)	Fill factor (FF)	$\eta$ (%)	
TiO <sub>2</sub>	Pt-RGO	14.3	0.74	59.5	6.37	5.64
	Pt	14.5	0.72	59.1	6.21	5.58
	RGO	10.5	0.69	26.8	1.95	1.50
Ag-TiO <sub>2</sub>	Pt-RGO	15.4	0.86	60.8	8.02	7.22
	Pt	15.1	0.84	61.4	7.73	6.80

<sup>a</sup> Short-circuit photocurrent densities ( $J_{SC}$  cm<sup>-2</sup>), open-circuit voltage ( $V_{OC}$ ) and efficiency ( $\eta$ ).

barrier exists at their interface.<sup>33</sup> The possible electron transfer pathways and formation of Schottky barrier are shown in Scheme 1. Under light illumination, the electrons from excited N719 dyes are injected to the Ag NPs on TiO<sub>2</sub> surface which results in accumulation of electrons in Ag NPs. As a result, the Fermi level of the Ag NPs shifted closer to the conduction band (CB) of TiO<sub>2</sub> in the Ag-TiO<sub>2</sub> nanocomposites which is responsible for the increase in  $V_{OC}$ . To the best of our knowledge, such a significant enhancement in the  $V_{OC}$  in presence of Ag NPs has not been reported earlier. Time resolved microwave conductivity (TRMC) studies have shown that electrons can be injected from Ag NPs to the CB of TiO<sub>2</sub> (ref. 23) in order to establish

charge equilibrium in the system. In contrast, the electrons at the CB of the TiO<sub>2</sub> cannot reverse their path to recombine with the oxidized dye or electrolyte due to the presence of Schottky barrier which results in enhanced efficiency of the device. In addition to the enhancement in  $V_{OC}$ , photocurrent also increases (14.5 to 15.1 mA cm<sup>-2</sup>) in case of Ag-TiO<sub>2</sub> nanocomposite which is well documented in the literature.<sup>10,11b</sup> This is due to an increase in effective absorption cross section of the dye (N719) and a modest increase in the framework surface area.

After the successful demonstration of Ag-TiO<sub>2</sub> as a photoanode, the counter electrode has been modified with Pt@RGO



Scheme 1 Schematic presentation of the dye-sensitized solar cell consists of Ag-TiO<sub>2</sub> photoanode and Pt@RGO counter electrode. Lower panel shows the energy level diagram.

Table 2 Dynamics of photovoltage transients of DSSCs fabricated using different active and counter electrodes<sup>a</sup>

Active electrode	Counter electrode	$\tau_1$ (s)	$\tau_2$ (s)	$\tau_3$ (s)	$\tau_{\text{avg}}$ (s)
TiO <sub>2</sub>	Pt-RGO	0.09 (48.5%)	1.28 (16.9%)	10.08 (34.6%)	3.74
	Pt	0.08 (32.4%)	0.39 (19.9%)	3.78 (47.7%)	1.91
Ag-TiO <sub>2</sub>	Pt-RGO	0.26 (25.7%)	1.67 (19.2%)	27.77 (55.1%)	15.68
	Pt	0.16 (30.2%)	1.17 (24.3%)	9.99 (45.5%)	4.87

<sup>a</sup> Numbers in the parenthesis indicate relative weightages.

to reduce the Pt loading as well as optimization of the catalytic activity. The amount of Pt in the Pt@RGO nanocomposite (2  $\mu\text{g}$  in each CE) is 10 times smaller than that of the standard Pt counter electrode (20  $\mu\text{g}$  in each CE) which lowers the cost and makes it viable for large scale commercial utilization. Although the amount of Pt decreases, the catalytic activity of Pt@RGO is comparable or slightly higher than the Pt only. The DSSCs with Ag-TiO<sub>2</sub> photoanode along with Pt@RGO and Pt counter electrode show energy conversion efficiency of 8.02% and 7.73%, respectively. The effect of CE on DSSC performance is dictated by the electrical conductivity and electrocatalytic activity in the reduction of triiodide to iodide.<sup>34</sup> In case of Pt@RGO, the catalytic activity of Pt and high electron conductivity of the stable support material RGO are synergistically combined owing to more interfacial active sites. The combination of Pt@RGO with bare TiO<sub>2</sub> as photoanode also exhibits slightly higher efficiency ( $\eta = 6.37\%$ ) than the Pt alone as CE ( $\eta = 6.21\%$ ). However, using control RGO as CE with TiO<sub>2</sub> as photoanode showed lower efficiency of 1.95%. In order to investigate the light harvesting by the N719 dye, the incident photon to current conversion efficiency (IPCE) of the cells were monitored as shown in Fig. 4b. The spectra collected from different cells show good agreement between the wavelength of photocurrent maximum and N719 absorption maximum ( $\lambda_{\text{max}} = 520 \text{ nm}$ ), signifying that the N719 sensitizers on the photoanode surface are indeed responsible for photocurrent generation. The trend in the photocurrent responses is consistent with the short circuit currents of the corresponding cells as shown in Fig. 4a.  $J_{\text{SC}}$  value of a cell can be estimated from the integrated area under the IPCE curve.<sup>35</sup> The  $J_{\text{SC}}$  values calculated from IPCE curves are found to be less compared to that obtained from the  $I$ - $V$  measurements. The difference in the  $J_{\text{SC}}$  values is due to the difference in the light intensity or power ( $\text{mW cm}^{-2}$ ) used for the two measurements. The  $I$ - $V$  characteristics were measured under 1 sun condition (100  $\text{mW cm}^{-2}$ , AM 1.5 simulated illuminations from AAA certified solar simulator), whereas the IPCE measurements were performed under monochromatic light illumination from dual light (tungsten and xenon) sources using a monochromator. Thus the light intensity or power falling on DSSC at a given wavelength during IPCE measurement is much lower than that of the  $I$ - $V$  measurements. The observation is consistent with the reported literature.<sup>35</sup>

In order to investigate the lifetime of accumulated charges at the photoanode, the decay of open circuit voltage has been monitored for different cells in the dark following a brief period of illumination. Upon visible light illumination, the excited

sensitizers inject electrons into TiO<sub>2</sub> electrode. The accumulated electrons in the TiO<sub>2</sub> drives the Fermi level to the more negative potential which reflects in the photovoltage enhancement. The forward electron injection from sensitizer to TiO<sub>2</sub> is terminated upon stopping the illumination, thus discharging of electrons occurs through the back electron transfer or recombination with the oxidized electrolytes. The open circuit voltage decay reflects the timescales for the recombination processes. Fig. 4c shows the decay profiles of different DSSCs fabricated using Ag-TiO<sub>2</sub> and TiO<sub>2</sub> as photoanode, Pt@RGO and Pt as CE. The fitted timescales are presented in Table 2. The Ag-TiO<sub>2</sub> photoanode in combination with Pt@RGO CE exhibit a remarkably slow rate of voltage decay (15.68 s) compared to the bare TiO<sub>2</sub> photoanode (3.74 s). This is due to the storage of electrons in Ag NPs<sup>23</sup> which prevents recombination with the oxidized electrolytes. This observation is consistent with the enhanced photovoltage in the presence of Ag-TiO<sub>2</sub> as a photoanode. The Pt@RGO CE in combination with TiO<sub>2</sub> photoanode shows slower decay with a lifetime of 3.74 s compare to the Pt CE (1.91 s). This can be attributed to the higher catalytic activity of Pt@RGO than Pt only at the CE in regenerating the oxidized electrolyte which in turn reduces the recombination processes. The stability of the DSSCs fabricated using Ag-TiO<sub>2</sub> photoanode and Pt@RGO CE, the photocurrent-voltage characteristics were monitored for 240 h. Fig. 5a depicts the change in short circuit current and open circuit voltage with time. Initially the  $J_{\text{SC}}$  decreases but after few days it is stable for a long period. The  $V_{\text{OC}}$  is very stable during the experimental time window which can be attributed to the stability of the Ag-TiO<sub>2</sub> photoanode. It is reported that the Ag NPs are easily damaged under oxidizing conditions.<sup>36</sup> However, our observation suggests that the Ag modified TiO<sub>2</sub> photoanode are stable which is consistent with the reported literature.<sup>10,11</sup> The fill factor and overall efficiency of the DSSCs are also consistent with time as shown in Fig. 5b.

In order to investigate the electronic and ionic processes in DSSCs, electrochemical impedance spectroscopy (EIS) were performed. As shown in Fig. 6a, the Nyquist plot features two semicircles, one in the high frequency region and the other one in the intermediate frequency region. The semicircle in the high frequency region can be attributed to the charge transfer at counter electrode while the semicircle in the intermediate frequency region is associated with the electron transport in the mesoscopic TiO<sub>2</sub> film and back reaction at the TiO<sub>2</sub>/electrolyte interface. The Nyquist plots are fitted using the equivalent circuit shown in Fig. 6b and the parameters are summarized in Table 3. The  $R_2$  value represents the interfacial recombination

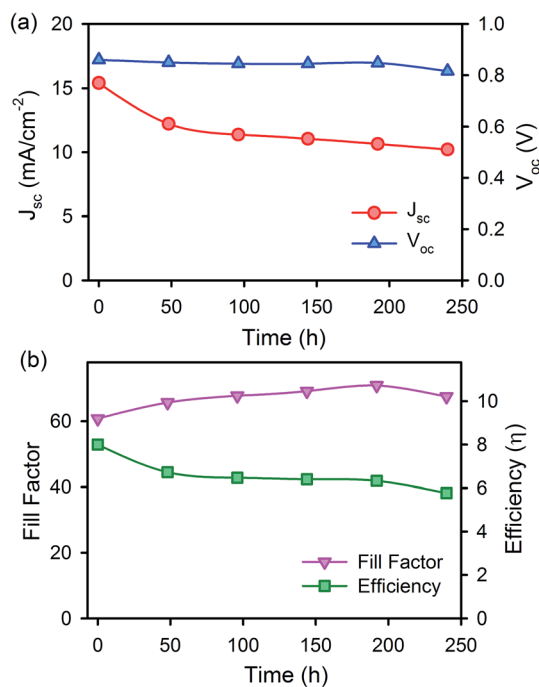


Fig. 5 Stability of the device. Plot of (a)  $J_{sc}$  and  $V_{oc}$ , (b) fill factor and efficiency of the DSSC fabricated using Ag-TiO<sub>2</sub> photoanode and Pt@RGO CE with time.

resistance at TiO<sub>2</sub>/electrolyte interface. The  $R_2$  value for Ag-TiO<sub>2</sub> photoanode (72.1  $\Omega$ ) is greater than that of the bare TiO<sub>2</sub> photoanode (12.6  $\Omega$ ) which can be attributed to the less charge recombination from Ag-TiO<sub>2</sub> photoanode to the triiodide ions in the electrolyte.<sup>11a</sup> The observation is consistent with the

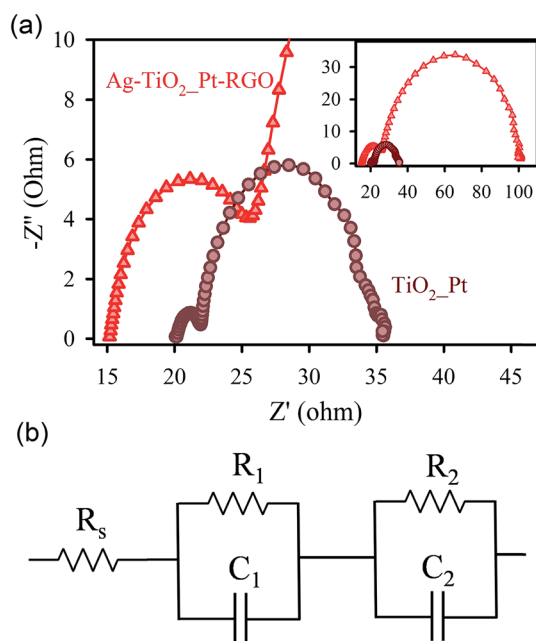


Fig. 6 EIS of the device. (a) Nyquist plots of different cells. Inset shows the full region. (b) Equivalent circuit model that was used to fit the EIS spectra.

Table 3 EIS parameters of DSSCs fabricated using different active and counter electrodes

Active electrode	Counter electrode	$R_s$ ( $\Omega$ )	$R_1$ ( $\Omega$ )	$R_2$ ( $\Omega$ )
Ag-TiO <sub>2</sub>	Pt-RGO	15.5	11.0	72.1
TiO <sub>2</sub>	Pt	20.3	1.9	12.6

slower photovoltage decay of the DSSC with Ag-TiO<sub>2</sub> photoanode as shown in Fig. 4c. This confirms that Ag NPs act as electron-hole separator due to the formation of Schottky barrier at the Ag-TiO<sub>2</sub> interface which prevents recombination with the oxidized electrolytes.<sup>33</sup> The  $R_1$  value represents the charge transfer resistance at the CE interface *i.e.* the catalytic activity of the electrode for reducing triiodide ions. The  $R_1$  value for Pt CE (1.9  $\Omega$ ) is less than that of the Pt@RGO CE (11.0  $\Omega$ ). Thus the Pt CE prepared by drop casting method exhibits slightly higher catalytic activity than that of the Pt@RGO CE as observed from EIS spectra<sup>21a</sup> which can be attributed to the 10 times lower Pt content in Pt@RGO CE than that of the Pt CE. However, the device performance of the Pt@RGO CE is comparable or slightly higher than Pt CE as shown in Fig. 4a which decreases the cost of CE significantly.

## 4. Conclusion

In summary, we have successfully utilized Ag modified TiO<sub>2</sub> (Ag-TiO<sub>2</sub>) as photoanode material in dye sensitized solar cell. On the other hand, we have demonstrated a facile synthesis of Pt NPs supported on RGO (Pt@RGO) surface by simple photo-reduction method without using chemical reducing or stabilizing agents. The quantity of Pt in the Pt@RGO nanocomposite is 10 times lower than that of the Pt counter electrode which reduces the cost and makes it viable for large scale commercial utilization. The combination of Ag-TiO<sub>2</sub> as photoanode and Pt@RGO as counter electrode leads to a light to electrical energy conversion with an overall efficiency of 8%. An enhancement of around 16% in the photovoltage ( $V_{oc}$ ) is observed in case of Ag-TiO<sub>2</sub> at photoanode compared to that of the bare TiO<sub>2</sub>, which can be attributed to the shifting of the quasi-Fermi level of the TiO<sub>2</sub> photoanode close to the conduction band in the presence of Ag NPs due to the formation of Schottky barrier at Ag-TiO<sub>2</sub> interface. Moreover, Pt@RGO is found to be more efficient than Pt only as CE due to the catalytic activity of Pt and high electron conductivity of the stable support material RGO. These advantages are synergistically combined owing to the large number of active interfacial sites. The open circuit voltage decay profiles show remarkably slow rate of electron recombination from Ag-TiO<sub>2</sub> photoanode to the oxidized electrolyte. The present study holds great promise for low cost, large scale fabrication of efficient solar devices.

## Acknowledgements

P. K. thanks CSIR (India) for fellowship. We thank DST (India) for financial grants DST-TM-SERI-2k11-103 and SB-S1-PC-011-

2013. We also thank DAE (India) for financial grant, 2013-37P-73-BRNS. PL and BL thank the DFG Research Training Group GrK1952/1 NanoMet, "Metrology for Complex Nanosystems" and the NTH-School "Contacts in Nanosystems".

## References

- (a) B. O'Regan and M. Grätzel, *Nature*, 1991, **353**, 737–740; (b) A. Yella, H.-W. Lee, H. N. Tsao, C. Yi, A. K. Chandiran, M. K. Nazeeruddin, E. W.-G. Diau, C.-Y. Yeh, S. M. Zakeeruddin and M. Grätzel, *Science*, 2011, **334**, 629–634; (c) S. Mathew, A. Yella, P. Gao, R. Humphry-Baker, F. E. Curchod/Basile, N. Ashari-Astani, I. Tavernelli, U. Rothlisberger, K. Nazeeruddin/Md and M. Grätzel, *Nat. Chem.*, 2014, **6**, 242–247; (d) M. Grätzel, *J. Photochem. Photobiol., C*, 2003, **4**, 145–153; (e) M. Grätzel, *Acc. Chem. Res.*, 2009, **42**, 1788–1798; (f) M. Graetzel, R. A. J. Janssen, D. B. Mitzi and E. H. Sargent, *Nature*, 2012, **488**, 304–312; (g) K. Lee, S. W. Park, M. J. Ko, K. Kim and N.-G. Park, *Nat. Mater.*, 2009, **8**, 665–671.
- (a) H. Wang, B. Wang, J. Yu, Y. Hu, C. Xia, J. Zhang and R. Liu, *Sci. Rep.*, 2015, **5**, 9305; (b) S. S. Mali, C. A. Betty, P. N. Bhosale, P. S. Patil and C. K. Hong, *Sci. Rep.*, 2014, **4**, 5451.
- (a) Y. Duan, N. Fu, Q. Liu, Y. Fang, X. Zhou, J. Zhang and Y. Lin, *J. Phys. Chem. C*, 2012, **116**, 8888–8893; (b) X. Zhang, S.-T. Wang and Z.-S. Wang, *Appl. Phys. Lett.*, 2011, **99**, 113503.
- (a) J.-W. Shiu, Y.-C. Chang, C.-Y. Chan, H.-P. Wu, H.-Y. Hsu, C.-L. Wang, C.-Y. Lin and E. W.-G. Diau, *J. Mater. Chem. A*, 2015, **3**, 1417–1420; (b) C.-L. Wang, J.-Y. Hu, C.-H. Wu, H.-H. Kuo, Y.-C. Chang, Z.-J. Lan, H.-P. Wu, E. Wei-Guang Diau and C.-Y. Lin, *Energy Environ. Sci.*, 2014, **7**, 1392–1396.
- (a) H. N. Tsao, C. Yi, T. Moehl, J.-H. Yum, S. M. Zakeeruddin, M. K. Nazeeruddin and M. Grätzel, *ChemSusChem*, 2011, **4**, 591–594; (b) H. Nusbaumer, S. M. Zakeeruddin, J.-E. Moser and M. Grätzel, *Chem.–Eur. J.*, 2003, **9**, 3756–3763.
- (a) V.-D. Dao, N. T. Q. Hoa, L. L. Larina, J.-K. Lee and H.-S. Choi, *Nanoscale*, 2013, **5**, 12237–12244; (b) G.-r. Li, F. Wang, Q.-w. Jiang, X.-p. Gao and P.-w. Shen, *Angew. Chem., Int. Ed.*, 2010, **49**, 3653–3656; (c) P. Joshi, Y. Xie, M. Ropp, D. Galipeau, S. Bailey and Q. Qiao, *Energy Environ. Sci.*, 2009, **2**, 426–429.
- (a) K. Hara, T. Horiguchi, T. Kinoshita, K. Sayama, H. Sugihara and H. Arakawa, *Sol. Energy Mater. Sol. Cells*, 2000, **64**, 115–134; (b) S. Ito, T. Kitamura, Y. Wada and S. Yanagida, *Sol. Energy Mater. Sol. Cells*, 2003, **76**, 3–13.
- (a) S. D. Standridge, G. C. Schatz and J. T. Hupp, *J. Am. Chem. Soc.*, 2009, **131**, 8407–8409; (b) Y. Li, H. Wang, Q. Feng, G. Zhou and Z.-S. Wang, *Energy Environ. Sci.*, 2013, **6**, 2156–2165; (c) C. Andrei, E. Lestini, S. Crosbie, C. de Frein, T. O'Reilly and D. Zerulla, *PLoS One*, 2014, **9**, e109836; (d) S. Linic, P. Christopher and D. B. Ingram, *Nat. Mater.*, 2011, **10**, 911–921; (e) S. Sarkar, A. Makhil, T. Bora, S. Baruah, J. Dutta and S. K. Pal, *Phys. Chem. Chem. Phys.*, 2011, **13**, 12488–12496; (f) T. Bora, H. H. Kyaw, S. Sarkar, S. K. Pal and J. Dutta, *Beilstein J. Nanotechnol.*, 2011, **2**, 681–690; (g) Z. Hai, N. El Kolli, D. B. Uribe, P. Beaunier, M. Jose-Yacamán, J. Vigneron, A. Etcheberry, S. Sorgues, C. Colbeau-Justin, J. Chen and H. Remita, *J. Mater. Chem. A*, 2013, **1**, 10829–10835.
- (a) S. Sardar, P. Kar, S. Sarkar, P. Lemmens and S. K. Pal, *Sol. Energy Mater. Sol. Cells*, 2015, **134**, 400–406; (b) S. Sardar, S. Sarkar, M. T. Z. Myint, S. Al-Harhi, J. Dutta and S. K. Pal, *Phys. Chem. Chem. Phys.*, 2013, **15**, 18562–18570; (c) S. Sardar, P. Kar and S. K. Pal, *J. Mat. NanoSci.*, 2014, **1**, 12–30; (d) S. Ghosh, A. H. Khan and S. Acharya, *J. Phys. Chem. C*, 2012, **116**, 6022–6030.
- N. C. Jeong, C. Prasittichai and J. T. Hupp, *Langmuir*, 2011, **27**, 14609–14614.
- (a) K. Guo, M. Li, X. Fang, X. Liu, B. Sebo, Y. Zhu, Z. Hu and X. Zhao, *J. Power Sources*, 2013, **230**, 155–160; (b) S.-J. Lin, K.-C. Lee, J.-L. Wu and J.-Y. Wu, *Sol. Energy*, 2012, **86**, 2600–2605; (c) M. Sun, W. Fu, H. Yang, Y. Sui, B. Zhao, G. Yin, Q. Li, H. Zhao and G. Zou, *Electrochem. Commun.*, 2011, **13**, 1324–1327; (d) S. H. Hwang, H. Song, J. Lee and J. Jang, *Chem.–Eur. J.*, 2014, **20**, 12974–12981.
- H. Choi, Y.-S. Chen, K. G. Stamplecoskie and P. V. Kamat, *J. Phys. Chem. Lett.*, 2015, **6**, 217–223.
- L. Bay, K. West, B. Winther-Jensen and T. Jacobsen, *Sol. Energy Mater. Sol. Cells*, 2006, **90**, 341–351.
- (a) N. Robertson, *Angew. Chem., Int. Ed.*, 2006, **45**, 2338–2345; (b) E. Olsen, G. Hagen and S. Eric Lindquist, *Sol. Energy Mater. Sol. Cells*, 2000, **63**, 267–273.
- K. S. Novoselov, A. K. Geim, S. V. Morozov, D. Jiang, Y. Zhang, S. V. Dubonos, I. V. Grigorieva and A. A. Firsov, *Science*, 2004, **306**, 666–669.
- (a) H. Wang and Y. H. Hu, *Energy Environ. Sci.*, 2012, **5**, 8182–8188; (b) S. G. Hashmi, J. Halme, Y. Ma, T. Saukkonen and P. Lund, *Adv. Mater. Interfaces*, 2014, **1**, 1300055.
- X. Xu, D. Huang, K. Cao, M. Wang, S. M. Zakeeruddin and M. Grätzel, *Sci. Rep.*, 2013, **3**, 1489.
- M.-Y. Yen, C.-C. Teng, M.-C. Hsiao, P.-I. Liu, W.-P. Chuang, C.-C. M. Ma, C.-K. Hsieh, M.-C. Tsai and C.-H. Tsai, *J. Mater. Chem.*, 2011, **21**, 12880–12888.
- V. Tjoa, J. Chua, S. S. Pramana, J. Wei, S. G. Mhaisalkar and N. Mathews, *ACS Appl. Mater. Interfaces*, 2012, **4**, 3447–3452.
- R. Bajpai, S. Roy, P. Kumar, P. Bajpai, N. Kulshrestha, J. Rafiee, N. Koratkar and D. S. Misra, *ACS Appl. Mater. Interfaces*, 2011, **3**, 3884–3889.
- (a) F. Gong, H. Wang and Z.-S. Wang, *Phys. Chem. Chem. Phys.*, 2011, **13**, 17676–17682; (b) H. Gong, S. Park, S.-S. Lee and S. Hong, *Int. J. Precis. Eng. Manuf.*, 2014, **15**, 1193–1199.
- Q. Wang, M. Song, C. Chen, W. Hu and X. Wang, *ChemPlusChem*, 2012, **77**, 432–436.
- E. Grabowska, A. Zaleska, S. Sorgues, M. Kunst, A. Etcheberry, C. Colbeau-Justin and H. Remita, *J. Phys. Chem. C*, 2013, **117**, 1955–1962.
- S. Ghosh, H. Remita, P. Kar, S. Choudhury, S. Sardar, P. Beaunier, P. S. Roy, S. K. Bhattacharya and S. K. Pal, *J. Mater. Chem. A*, 2015, **3**, 9517–9527.
- F. Dehouche, P. Archirel, H. Remita, N. Brodie-Linder and A. Traverse, *RSC Adv.*, 2012, **2**, 6686–6694.

- 26 A. Grinou, Y. Yun, S. Cho, H. Park and H.-J. Jin, *Materials*, 2012, **5**, 2927–2936.
- 27 C. Zhang, X. Zhu, Z. Wang, P. Sun, Y. Ren, J. Zhu, J. Zhu and D. Xiao, *Nanoscale Res. Lett.*, 2014, **9**, 490.
- 28 P. Hasin, M. A. Alpuche-Aviles and Y. Wu, *J. Phys. Chem. C*, 2010, **114**, 15857–15861.
- 29 K. N. Kudin, B. Ozbas, H. C. Schniepp, R. K. Prud'homme, I. A. Aksay and R. Car, *Nano Lett.*, 2008, **8**, 36–41.
- 30 S. Stankovich, D. A. Dikin, R. D. Piner, K. A. Kohlhaas, A. Kleinhammes, Y. Jia, Y. Wu, S. T. Nguyen and R. S. Ruoff, *Carbon*, 2007, **45**, 1558–1565.
- 31 W. Nie, R. C. Coffin and D. L. Carroll, *Int. J. Photoenergy*, 2013, **2013**, 829463.
- 32 H. Wu and L. S. Wang, *J. Chem. Phys.*, 1997, **107**, 8221–8228.
- 33 Z. Zhang and J. T. Yates, *Chem. Rev.*, 2012, **112**, 5520–5551.
- 34 N. Papageorgiou, *Coord. Chem. Rev.*, 2004, **248**, 1421–1446.
- 35 R. K. Kokal, P. Naresh Kumar, M. Deepa and A. K. Srivastava, *J. Mater. Chem. A*, 2015, **3**, 20715–20726.
- 36 S. D. Standridge, G. C. Schatz and J. T. Hupp, *Langmuir*, 2009, **25**, 2596–2600.